Chemical Engineering Science 98 (2013) 173–185

Contents lists available at SciVerse ScienceDirect

Chemical Engineering Science

journal homepage: www.elsevier.com/locate/ces

Upscaling and microstructural analysis of the flow-structure relation perpendicular to random, parallel fiber arrays

K. Yazdchi *, S. Luding

Multi-Scale Mechanics, MESA+ Institute for Nanotechnology, Faculty of Engineering Technology, University of Twente, P.O. Box 217, 7500 AE Enschede, The Netherlands

HIGHLIGHTS

- Voronoi/Delaunay tessellations are used to characterize the microstructure.
- Relate macroscopic permeability to microscopic fiber arrangements.
- Permeability and local bond orientational parameter deviate exponentially from random case.
- Verify the validity of Darcy's law at various length scales and porosities.

GRAPHICAL ABSTRACT

Variation of average horizontal fluid velocity at porosity $\varepsilon = 0.6$ using (a) Delaunay triangulation and (b) Voronoi polygons as an averaging area.

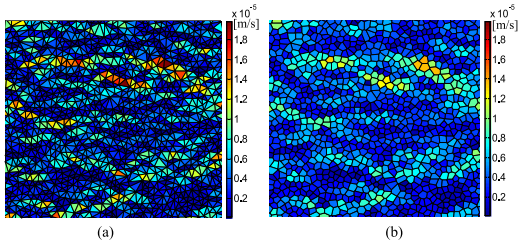

ARTICLE INFO

Article history:
Received 10 December 2012
Received in revised form
22 April 2013
Accepted 26 April 2013
Available online 3 May 2013

Keywords:
Darcy's law
Porous media
Delaunay tessellation
Numerical analysis
Multiphase flow
Microstructure

ABSTRACT

Owing largely to multiscale heterogeneity in the underlying fibrous structure, the physics of fluid flow in and through fibrous media is incredibly complex. Using fully resolved finite element (FE) simulations of Newtonian, incompressible fluid flow perpendicular to the fibers, the macroscopic permeability is calculated in the creeping flow regime for arrays of random, ideal, perfectly parallel fibers.

On the micro-scale, several order parameters, based on Voronoi and Delaunay tessellations, are introduced to characterize the structure of the randomly distributed, parallel, non-overlapping fiber arrays. In particular, by analyzing the mean and the distribution of the topological and metrical properties of Voronoi polygons, we observe a smooth transition from disorder to (partial) order with decreasing porosity, i.e., increasing packing fraction.

On the macro-scale, the effect of fiber arrangement and local crystalline regions on the macroscopic permeability is discussed. For both permeability and local bond orientation order parameter, the deviation from a fully random configuration can be well represented by an exponential term as function of the mean gap width, which links the macro- and the micro-scales.

Finally, we verify the validity of the, originally, macroscopic Darcy's law at various smaller length scales, using local Voronoi/Delaunay cells as well as uniform square cells, for a wide range of porosities. At various cell sizes, the average value and probability distributions of macroscopic quantities, such as superficial fluid velocity, pressure gradient or permeability, are obtained. These values are compared with the macroscopic permeability in Darcy's law, as the basis for a hierarchical upscaling methodology.

1. Introduction

Fluid flow through fibrous materials has a wide range of applications including, composite materials, fuel cells, heat exchangers, (biological) filters and transport of ground water and pollutants (Bird et al., 2001). Permeability, i.e. the ability of the fluid to flow, is perhaps the most important property in their manufacturing.

* Corresponding author. Tel.: +31 534894212.
E-mail addresses: kyazdchi@gmail.com (K. Yazdchi), s.luding@utwente.nl (S. Luding).

0009-2509/$ - see front matter © 2013 Elsevier Ltd. All rights reserved.
http://dx.doi.org/10.1016/j.ces.2013.04.049

Prediction of the macroscopic permeability is a longstanding but still challenging problem that dates back to the work of Happel (1959) and Kuwabara (1959) with more recent contributions by Sangani and Acrivos (1982), Drummond and Tahir (1984), Gebart (1992) and Bruschke and Advani (1993). Most of these models/predictions are complex with limited range of validity. For example, Gebart (1992) presented an expression for the transverse permeability based on the lubrication approximation valid for ordered structures, which are different from the generally disordered fibrous materials. For a review of the theory, predictability and limitations of these models see Yazdchi et al. (2012), Deen et al. (2007) Zhu et al. (2008) and references therein.

Based on the orientation of the fibers in space, fibrous structures can be categorized into three different classes: (i) 1D structure in which all fibers are parallel with each other (Sangani and Yao, 1988; Narvaez et al., 2013), (ii) 2D structure in which fibers lie in parallel planes with directional or random orientations (Sobera and Kleijn, 2006; Jaganathan et al., 2008) and (iii) 3D structures in which fibers are directionally or randomly oriented in space (Tomadakis and Robertson, 2005; Clague et al., 2000; Stylianopoulos et al., 2008; Tomadakis and Sotirchos, 1993). In general, macroscopic transport properties such as permeability (or e.g. the heat transfer coefficient) are functions of geometrical features of the porous medium; thus determination of exact transport properties for 3D real fibrous materials with random structures is very complex and in many cases not possible. However, several researchers have argued that, in principle, the permeability of random 2D and 3D media can be related to their values for 1D structures (Jackson and James, 1986; Tamayol and Bahrami, 2011; Mattern and Deen, 2007). Therefore, as basic step, to provide physical insight into the significance of the microscopic structure for the macroscopic transport properties, the transverse permeability of 1D random structures is investigated in the present study.

Darcy's law is the most widely used empirical relation for the calculation of the pressure drop across a homogeneous, isotropic and non-deformable porous medium. It states that, at the macroscopic level and the limit of creeping flow regimes, the pressure gradient ∇p, and the flow rate have a linear relation given by

$$-\nabla p = \frac{\mu}{K} U, \tag{1}$$

where μ and U are the viscosity and the horizontal superficial (discharge) velocity, respectively. The proportionality constant K, is called the permeability of the medium and it strongly depends on the microstructure (e.g. fiber/particle shape and arrangement, void connectivity and inhomogeneity of the medium) and porosity. Darcy's law was originally obtained from experiments (Lage and Antohe, 2000) and later formalized using upscaling (Whitaker, 1986), homogenization (Mei and Auriault, 1991) and volume averaging (Valdes-Parada et al., 2009) techniques. It has been shown that Darcy's law actually represents the momentum equation for Stokes flow averaged over a representative volume element (RVE). In fact, in this representation, all complicated interactions between fluid and solid (fibers) are lumped into the permeability (tensor), K.

The lack of a microscopic foundation has motivated the development of relationships between macroscopic parameters, like permeability, and microstructural parameters, like fiber arrangements, shape and orientation or tortuosity (flow path). Chen and Papathanasiou (2007, 2008) computationally investigated the flow across randomly distributed unidirectional arrays using the boundary element method (BEM) and found a direct correlation between permeability and the mean nearest inter-fiber spacing. Papathanasiou (1996) performed a similar study for unidirectional square arrays of fiber clusters (tows) using the BEM. His employed unit cells are characterized by two porosities: (i) inter-tow porosity, determined by the macroscopic spatial arrangement of the tows, and (ii) intra-tow porosity, determined by the fiber concentration inside each tow. He showed that the effective permeability of assemblies of fiber clusters depends strongly on the intra-tow porosity only at low inter-tow porosity. In a recent study, Yazdchi et al. (2012) proposed a power law relation between the transverse permeability obtained from finite element (FE) simulations and the mean value of the shortest Delaunay triangulation (DT) edges, constructed using the centers of the fibers. For sedimentary rocks, especially sandstones, Katz and Thompson (1986) suggested, using percolation theory, a quadratic relation between permeability and microstructural descriptors for rocks, i.e. the critical pore diameter. Despite all these attempts, the effect of microscopic fiber arrangements/structures, controlled by the effective packing fraction, on macroscopic permeability is still unclear.

The objective of this paper is to (i) computationally investigate transverse flow through 1D, random fiber arrays in a wide range of porosities, (ii) understand and characterize the microstructure, i.e. the ordered and disordered states, using several order parameters, (iii) establish a relationship between macroscopic permeability and the microstructure of the fibrous materials and (iv) verify the validity of the empirical Darcy's law at various length scales and porosities. Our results can and will be used in more practically relevant hybrid or coupled codes with two-way coupling between the fibers and the fluid to more mimic a real fiber-tow production/impregnation process as a big step toward the same for the most general full 3D random structures.

To this end, the algorithm used to build the initial fiber configurations and the numerical finite element (FE) procedure for solving flow/momentum equations are presented in Section 2. In Section 3, the geometrical (Voronoi tessellation) and bond orientational order parameters are introduced to quantify the microstructure. In particular, the transition from disordered to ordered regimes is discussed in detail. The connection between structural (dis)order and macroscopic permeability is explained using shortest Delaunay triangulation edges in Section 4. Finally, the validity of Darcy's law at different length scales is investigated by dividing the system into both smaller uniform cells and irregular Voronoi/Delaunay polygons/triangles in Section 5. The paper is concluded in Section 6 with a summary and outlook for future research and applications.

2. Mathematical formulation and methodology

A Monte Carlo (MC) approach was used to generate $N=3000$ randomly distributed, non-overlapping fiber arrays in a square domain with length, L. Given an initial fiber configuration on a triangular lattice, the MC procedure perturbs fiber center locations in randomly chosen directions and magnitudes (Chen and Papathanasiou, 2007, 2008). The perturbation was rejected if it leads to overlap with a neighboring fiber (up to 10^4 perturbations were used in our simulations). With this procedure, we were able to generate various packings at different porosities, $\varepsilon=1-N\pi d^2/(4L^2)$ with d the diameter of fibers, varying from dense/ordered ($\varepsilon=0.3$) to vary dilute/disordered ($\varepsilon=0.95$) regimes. Fig. 1 shows a schematic of such a packing; the fiber long axis is normal to the flow direction, at porosity $\varepsilon=0.6$. Due to wall/edge effects, only the center part of the system will be analyzed. The effect of several microstructural parameters such as method of generation, system size, wall/periodic boundaries have been discussed elsewhere (Yazdchi et al., 2012).

The FE software ANSYS® was used to calculate the horizontal superficial (discharge) velocity, U, from the results of our computer

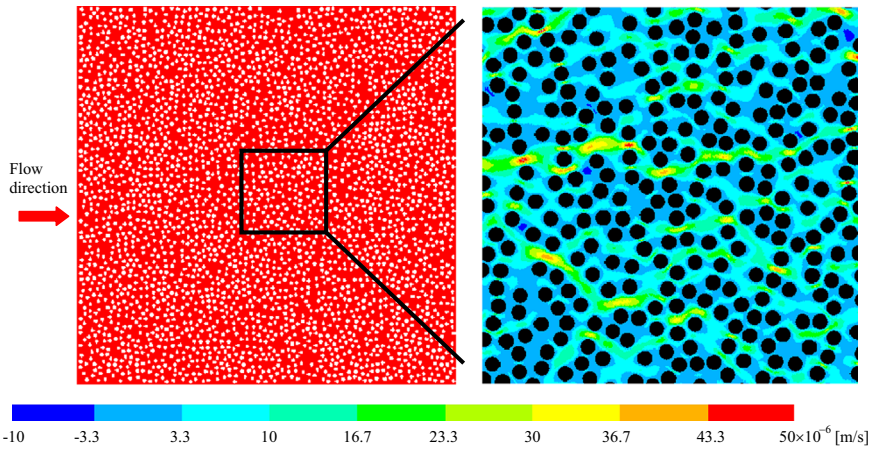

Fig. 1. Illustration of $N=3000$ randomly distributed fibers (particles) using a Monte Carlo procedure at porosity $\varepsilon=0.6$ with minimum inter-fiber distance $\Delta_{\min}=0.05$. The zoom shows the corresponding horizontal velocity field.

simulations as

$$U=\frac{1}{A}\int_{A_f} u dA=\frac{1}{L^2}\sum_e u_e A_e, \tag{2}$$

where A, A_f and u are the total area of the unit cell, the area of the fluid and the intrinsic fluid velocity, respectively. The subscript "e" indicates the corresponding quantity for each triangular element. Using Eq. (1), the permeability of the fibrous media can then be calculated. On the flow domain, the steady state Navier–Stokes equations combined with the continuity equations were discretized into an unstructured, triangular mesh. They were then solved using a segregated, sequential solution algorithm. The developed matrices from assembly of linear triangular elements are then solved based on a Gaussian elimination algorithm. Some more technical details are given in Yazdchi et al. (2011, 2012). At the left and right pressure- and at the top and bottom and surface of the particles no-slip boundary conditions, i.e. zero velocity is applied. Similar to Chen and Papathanasiou (2007, 2008), a minimal distance, $\Delta_{\min}=\delta_{\min}/d=0.05$ is needed in 2D to avoid complete blockage. We assigned a virtual diameter $d^*=d(1+\Delta_{\min})$ to each fiber, leading to the virtual porosity $\varepsilon^*=1-(1-\varepsilon)(1+\Delta_{\min})^2$. While ε represents the porosity available for the fluid, ε^* (i.e. porosity with artificially enlarged particles) is actually used for packing generation. The effect of $\Delta_{\min}$ on fiber arrangement and macroscopic permeability is investigated in Yazdchi et al. (2012). The mesh size effect was examined by comparing the simulation results for different resolutions (data not shown here). The number of elements varied from 5×10^5 to 10^6 depending on the porosity regime. The lower the porosity the more elements are needed in order to resolve the flow within the neighboring fibers. The horizontal velocity field of such a simulation at porosity $\varepsilon=0.6$ is shown in Fig. 1. We observed some dominant flow channels, especially at low porosities, which contribute over-proportionally to the fluid transport. More discussions on quantifying these channels and their relation to the macroscopic permeability are provided in Section 4.

3. Microstructure characterization

An important element in understanding of fibrous materials is the description of the local fiber arrangements and the possible correlations between their positions. The classical way for characterizing the structure, like disorder to order transition, is by inspection of its radial distribution function $g(r)$, which is defined as the probability of finding the center of a fiber inside an annulus of internal radius r and thickness dr (Chen and Papathanasiou, 2007, 2008; Yazdchi et al., 2012; Reis et al., 2006). As the crystallization begins to occur at moderate porosities, peaks appear for values of r which correspond to the second (linear) neighbors in a hexagonal lattice in 2D or a FCC or HCP arrangements in 3D. The complete randomness of the fiber distribution on larger scale will assure that $g(r)=1$. However, as pointed out by Rintoul and Torquato (1996), this method is unsatisfying for two reasons: on the one hand the absence of clear peaks does not necessarily mean the absence of crystallization, and on the other hand it is difficult to determine exactly when the peak appears. In this section, we propose another way to characterize more quantitatively the microstructure of 2D, non-overlapping fiber packings, namely by analyzing (i) the statistical geometry of the Voronoi/Delaunay tessellation and (ii) the bond orientational order parameter, in a wide range of porosities.

3.1. Voronoi diagram (VD)

The Voronoi tessellation can be used to study the local and/or global ordering of packings of discs/fibers in 2D. Motivation stems from their variety of applications in studying correlations in packings of spheres (Oger et al., 1996; Richard et al., 1999), analysis for crystalline solids and super-cooled liquids (Tsumuraya et al., 1993; Yu et al., 2005), the growth of cellular materials (Pittet, 1999), and the geometrical analysis of colloidal aggregation (Earnshaw et al., 1996) and plasma dust crystals (Zheng and Earnshaw, 1995). For a review of the theory and applications of Voronoi tessellations, see the books by Okabe et al. (1992) and Berg et al. (2008), and the surveys by Aurenhammer (1991) and Schliecker (2002).

For equal discs (i.e. a simplified 2D representation of unidirectional random fiber arrays), as considered here, given a set of two or more but a finite number of distinct points (generators) in the Euclidean plane, we associate all locations in that space with the closest member(s) of the point set with respect to the Euclidean distance. The result is a tessellation, called Voronoi diagram, of the plane into a set of regions associated with members of the point set, see thick red lines in Fig. 2. This construction is unique and fills the whole space with convex polygons. In a hexagonally close packed (densest) configuration, i.e. $\varepsilon^*_{hex}\equiv0.093$, the Voronoi tessellation consists of regular hexagons. It allows us to define the notion of "neighbor" without ambiguity for any packing fraction: two spheres/discs are neighbor if their Voronoi polyhedra share one face/edge. It can be easily generalized to radical tessellation for polydisperse assemblies of spheres (Richard et al., 1998) or

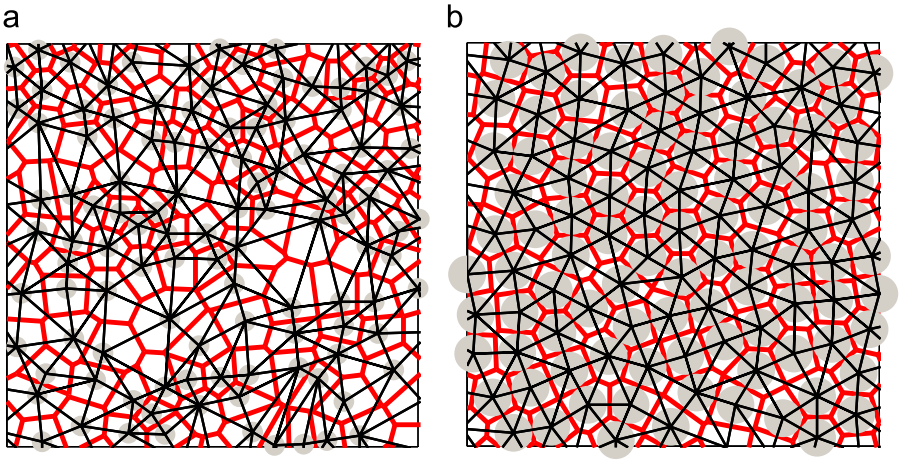

Fig. 2. Illustration of the Voronoi (red line) and Delaunay (black lines) tessellations for the center part of a system of identical discs/fibers at (a) dilute, $\varepsilon = 0.8$ and (b) dense, $\varepsilon = 0.4$ regimes for $\Delta_{\min} = 0.05$ (For interpretation of the references to color in this figure legend, the reader is referred to the web version of this article.).

discs (Gervois et al., 1995) by using the Laguerre distance between obstacles, which takes into account the size of each point species.

The Delaunay triangulation (DT) is the dual graph of the Voronoi diagram. This graph has a node for every Voronoi cell and has an edge between two nodes if the corresponding cells share an edge, see thin black lines in Fig. 2. DT cells are always triangles in 2D, and are thus typically smaller than Voronoi cells.

Recently, various studies have focused on the geometrical properties of Voronoi tessellations resulting from random point processes, i.e. $\varepsilon = 1$, to densely packed hard discs or spheres. In particular, Zhu et al. (2001) and Kumar and Kumaran (2005) observed that by decreasing the porosity the degree of randomness of the tessellation is decreased—the probability distribution functions (PDFs) of the statistical properties of the geometrical characteristics become more and more peaked and narrower—until the unique critical value of a regular tessellation, i.e. of hexagonal cells, is adapted.

In order to gain further insight into the relative arrangement of the Voronoi cells, their topological correlations and metric properties have been studied in the following. In particular, we focus on (i) the distribution and evolution of the number of faces, $p(n)$ together with their 2nd and 3rd moments and (ii) the shape and regularity (or isotropy) of the Voronoi polygons at different porosities.

3.1.1. Topological correlations for Voronoi tessellations

This section is dedicated to the study of the evolution of the probability distribution of n-sided polygons, $p(n)$ when changing the porosity. Note that only the information obtained from the inner fibers, which were at least 5 fiber diameters away from the walls, was included in our analysis. This treatment should satisfactorily eliminate the wall/edge effects up to high densities. To get better statistics, the results were averaged over 10 realizations with 10^4 MC perturbations. The two straightforward conservation laws are

$$\sum_n p(n) = 1 \quad \text{(normalization)}, \quad \text{and} \tag{3}$$

$$\sum_n np(n) = 6 \quad \text{(the average number of edges is 6)}, \tag{4}$$

as the consequence of the Euler theorem (Okabe et al., 1992; Smith, 1954). The distributions of the cell topologies, $p(n)$ of Voronoi tessellations, generated at various porosities are observed to follow a discretized and truncated Gaussian shape (not shown here). The perfectly ordered structure is manifested by hexagonal cells, i.e. $n=6$ and $p(n)=1$, and disorder/randomness shows up as the presence of cells with other than six sides (topological defects). The increase of disorder in the disc/fiber assemblies at high porosities leads to an increase of the topological defect concentration, i.e. a broadening of $p(n)$.

In the literature, both the topological defect concentration $1-p(6)$, and the variance (2nd central moment) $\mu_2 = \langle n^2\rangle - \langle n\rangle^2 \equiv \langle (n-\langle n\rangle)^2\rangle \equiv \sum_n p(n)(n-6)^2$ of the cell topologies, are used as measures of the degree of disorder (Miklius and Hilgenfeldt, 2012; Le Caer and Delannay, 1993; Lemaítre et al., 1991, 1993; Rivier, 1994). Lemaítre et al. (1993) were, to our knowledge, the first to suggest that the equation of state $\mu_2 = f(p(6))$ could be universal in mosaics. In this sense, all information about topological disorder in these systems is contained in $p(6)$. Astonishingly, Lemaítre's law holds very robustly for most of experimental, numerical, and analytical data (Gervois et al., 1992).

Fig. 3(a) shows the correlation between $p(6)$ and the topological variance μ_2 for different microstructures and at various porosities. In the ordered regime, i.e. $p(6) > 0.65$, mainly 5, 6 and 7 sided polygons with $p(5) \cong p(7) \cong (1-p(6))/2$ occur, and by applying the maximum entropy principle with the constraints in Eqs. (3) and (4) (Rivier, 1994), we obtain $\mu_2 = 1-p(6)$; it has the trivial virial expansion that corresponds to an ideal gas. By increasing the porosity, i.e. $\varepsilon > 0.45$ or $\varepsilon^* > 0.39$, one enters the disordered regime and $\mu_2 \cong 1/(2\pi p^2(6))$. Finally, in the limit of vanishing density ($\varepsilon = 1$), the fibers are randomly distributed and one has $p(6) \cong 0.3$ and $\mu_2 \cong 1.78$. This limit is obtained by analyzing the Voronoi polygons generated from 10^7 randomly distributed points. The transition porosity $\varepsilon_t^* \cong 0.39$ can be more clearly determined by plotting the third central moments of the n-sided polygon distributions, $\mu_3 = \langle (n-\langle n\rangle)\rangle^3$ against porosity, as shown in Fig. 3(b). Note that this value is still far above the random close packing limit $\varepsilon_{rcp}^* \cong 0.16$ (Berryman, 1983), as compared also to the minimum hexagonal lattice porosity $\varepsilon_{hex}^* \cong 0.093$, the freezing point $\varepsilon_f^* \cong 0.309$ (Alder and Wainwright, 1962) or the melting point $\varepsilon_m^* \cong 0.284$ (Alder and Wainwright, 1962).

3.1.2. Metric properties

The metrical properties of two-dimensional froths are often studied in terms of the average n-sided cell areas, $\langle A_n\rangle$ or the average cell perimeters, $\langle L_n\rangle$. Lewis's law (Lewis, 1931) and Desch's law (Desch, 1919) are two empirical relations which state that the average cell areas and perimeters vary linearly with n for certain systems, while for others nonlinear analogs have been observed (Le Caer and Delannay, 1993; Quilliet et al., 2008; Glazier et al., 1987). Only recently, using the local, correlation-free granocentric model approach with no free parameters, Miklius and Hilgenfeldt

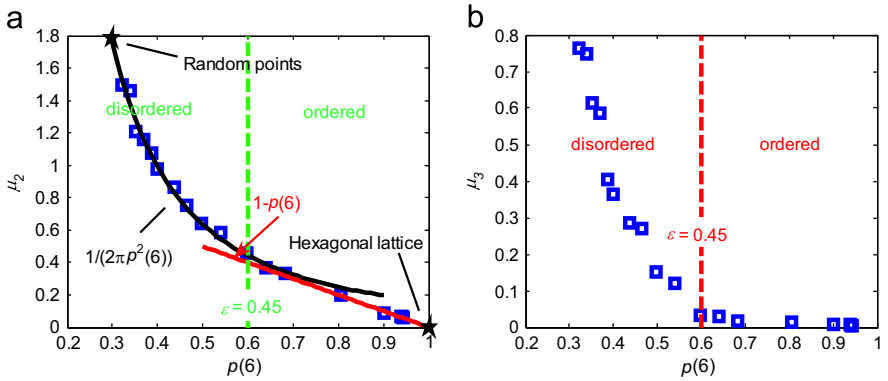

Fig. 3. (a) The correlation between $p(6)$ and the topological variance μ_2 for various structures and porosities. The analytical theories, represented by solid lines, are calculated by the Maxent method (Rivier, 1994). (b) Variation of the third moment of n-sided polygon distributions, μ_3 plotted against $p(6)$. The transition from order to disorder occurs at $\varepsilon_t \cong 0.45 (\varepsilon_t^* \cong 0.39)$.

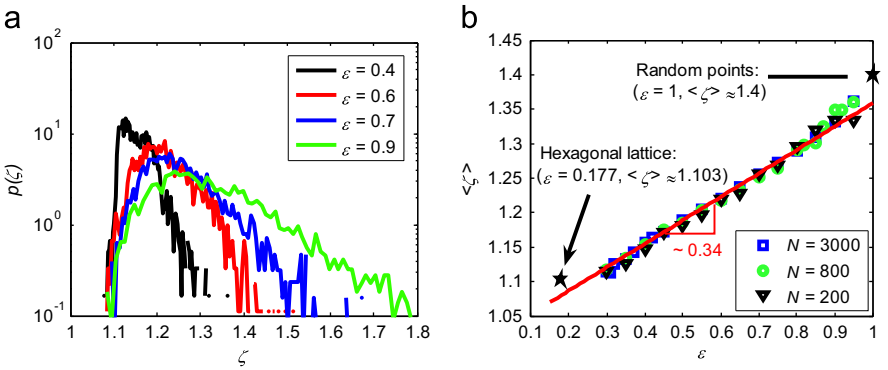

Fig. 4. (a) The probability distribution of the shape factor, ζ at different porosities. (b) Average shape factor plotted against porosity for different number of fibers/discs. The solid red line shows the best linear least square fit. All data are averaged over 10 realizations with 10^4 MC perturbations (For interpretation of the references to color in this figure legend, the reader is referred to the web version of this article.).

(2012) construct accurate analytical descriptions for these empirical laws in 2D and Clusel et al. (2009) in 3D.

Combining the cell area and its perimeters, we apply the concept of shape factor, to further quantify the shape/circularity of the Voronoi cells as

$$\zeta = \frac{L^2}{4\pi A}. \tag{5}$$

In this dimensionless representation, two Voronoi polygons can have the same number of sides, n, but different values of ζ (due to the irregularity of the polygons), since one of the advantages is that the shape factor, ζ is a continuous variable while n is discrete. This quantity was recently used to study crystallization of 2D systems, both in simulations (Moucka and Nezbeda, 2005) and experiments (Reis et al., 2006; Abate and Durian, 2006; Wang et al., 2010). By construction, $\zeta = 1$ for a perfect circle, and is larger for more rough or elongated shapes, like pentagons or heptagons. For a hexagonal lattice (densest packing) one has $\zeta_{hex} = 1.103$ and, in general, for a regular n-sided polygon $\zeta = (n/\pi)\tan(n/\pi)$.

The shape factor distributions, $p(\zeta)$ and the way they change with porosity are displayed in Fig. 4(a). For dilute systems (disordered regime), $p(\zeta)$ exhibits a broad and flat distribution with values above ζ_{hex}, maximum at about $\zeta \approx 1.25$ and an exponential tail. In this case, in fact, the particles are randomly distributed with no preferential type of polygons. At lower porosities, this peak progressively moves toward lower values, i.e. to more circular domains, and eventually bifurcates into two sharper peaks. Fig. 4(b) shows the average shape factor, $\langle\zeta\rangle$ taken over all polygons at different porosities for various system sizes (number of particles, N). The numerical results show that $\langle\zeta\rangle$ is not noticeably affected by system size. Interestingly, we observed that its value increases almost linearly with porosity (for $0.3 < \varepsilon < 0.85$). A similar linear dependence was observed for packing configurations obtained from a different generation algorithms, namely an energy minimization approach (Yazdchi et al., 2012), data not shown here. Unlike the data presented in Fig. 3, the trend does not indicate a change at the transition porosity $\varepsilon_t \cong 0.45$ ($\varepsilon_t^* \cong 0.39$), and therefore this is not a good criterion for detecting the order to disorder transition. Finally, in the limit of random point distributions one has $\langle\zeta\rangle \cong 1.4$. This value is obtained from 10^7 randomly distributed points.

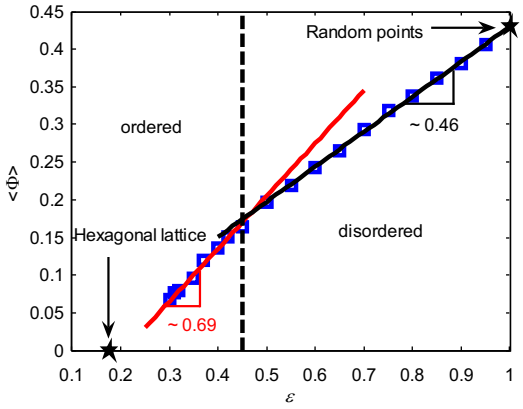

Fig. 5. Variation of average $\langle\Phi\rangle$ plotted against porosity. The solid lines show the best linear least square fits. Similar to the $\mu_2 = f(p(6))$ relation, the transition from order to disorder occurs at $\varepsilon_t \cong 0.45$ ($\varepsilon_t^* \cong 0.39$).

A drawback of the shape factor is that, with this definition, the regularity (or isotropy) of the Voronoi polygons cannot be

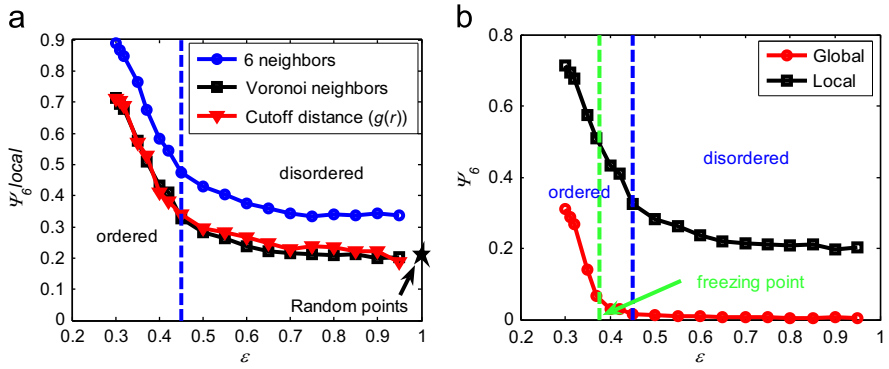

Fig. 6. (a) Illustration of the sensitivity of the local ψ_6^l to the nearest neighbor selection method. (b) Variation of the global, ψ_6^g and the local, ψ_6^l bond orientational order parameter plotted against porosity, using the Voronoi/Delaunay neighbors.

deduced. In other words, one has no information about the deviation of each vertex of a polygon from the principal axis. Therefore, we define a new dimensionless parameter, Φ as

$$\Phi = \left| \frac{I_1 - I_2}{I_1 + I_2} \right|, \tag{6}$$

where I_1 and I_2 are the area moments about the principal axes of a polygon. For all Voronoi shapes, Φ varies between zero and unity, although our numerical results show that it does not exceed a maximum value corresponding to a random cloud of points $\Phi \cong 0.43$ (see Fig. 5). For the polygons which are "isotropic", like hexagons, one has $I_1 \cong I_2$ and therefore $\Phi \cong 0$. Polygons which are stretched along one of their principal axes have larger values of Φ, with $\Phi = 1$ for as maximum as possible.

Fig. 5 shows the average $\langle \Phi \rangle$ taken over all polygons against porosity. As the porosity increases, the $\langle \Phi \rangle$ also increases, indicating a more anisotropic shape, until it reaches its maximum value for random points, i.e. $\Phi \cong 0.43$. Interestingly, two linear functions with different slopes can be fitted to the disordered and ordered regimes. Just as was observed in Fig. 3(b), the transition (crossing of the two lines) occurs at $\varepsilon_t \cong 0.45$ ($\varepsilon_t^* \cong 0.39$).

3.2. Bond orientational order parameter

The bond orientation angle, ψ_6, which is defined in terms of the nearest-neighbor bond angles, measures the hexagonal registry of nearest neighbors. This quantity has been used to detect local/global crystalline regions both in 2D and 3D, see for example Kumar and Kumaran (2006), Halperin and Nelson (1978), Jaster (1999), Kawasaki and Onuki (2011), Kansal et al. (2000) and references therein. The sixfold global bond-orientational order parameter of the 2D, non-overlapping fibrous system is defined as

$$\psi_6^g = \frac{1}{N} \left| \sum_{i=1}^{N} \frac{1}{n_i} \sum_{j=1}^{n_i} e^{6i\theta_{ij}} \right|, \tag{7}$$

where θ_{ij} is the angle between particle i and its neighbors j with respect to an arbitrary but fixed reference axis, and n_i denotes the number of nearest neighbors of particle i. ψ_6^g is sensitive to (partial) crystallization and increases significantly from $\psi_6^g \sim 0$ for a dilute system to $\psi_6^g = 1$ for a perfect hexagonal lattice.

A more local measure of orientational order can be obtained by evaluating the bond-orientational order of each particle individually, and then averaging over all particles to give

$$\psi_6^l = \frac{1}{N} \sum_{i=1}^{N} \frac{1}{n_i} \left| \sum_{j=1}^{n_i} e^{6i\theta_{ij}} \right|. \tag{8}$$

such a local measure of order is more sensitive to small local crystalline regions within a packing compared to its global counterpart ψ_6^g, and thus avoids the possibility of "destructive" interference between differently oriented crystalline regions (Kansal et al., 2000). Since ψ_6^g and ψ_6^l differ in the averaging procedure, they yield different numerical values.

The first step in evaluating ψ_6, which was not precisely addressed before, is to detect the nearest neighbors of a reference particle i. Fig. 6(a) shows the sensitivity of the local ψ_6^l to the number of nearest neighbors obtained from (i) a cutoff distance taken from the first minimum in the radial distribution function, $g(r)$ (ii) Voronoi/Delaunay neighbors or (iii) using up to and including the 6 nearest neighbors. Although the average of Voronoi neighbors is 6 (Eq. (4)), the local ψ_6^l calculated on the Voronoi neighbors have lower values than the ones calculated from the 6 nearest neighbors. Voronoi neighbors and the neighbors based on the cutoff distance result in almost the same numerical values. For decreasing porosity, the local ψ_6^l rises sharply at $\varepsilon_t \cong 0.45$, indicating highly correlated local order. However, the transition is not sharp, since the order parameter increases slightly for $\varepsilon \leq 0.7$. In very dilute regimes, the local order parameter $(\psi_6^l)_{ran} \cong 0.21$ is larger than zero, leading to the interesting question of whether there is a minimum, nonzero value of this parameter for a random system. A possible answer is that in random non-overlapping fiber arrays, there are still some local crystalline regions, due to the lack of geometric frustration, which are not correlated. In Fig. 6(b) the numerical values of the global, ψ_6^g and local, ψ_6^l are compared and plotted against porosity, using the Voronoi neighbors. Unlike the local definition, the global ψ_6^g is almost zero in the disordered regime, due to phase cancellations, and increases sharply at $\varepsilon \cong 0.37$, i.e. the freezing point (Alder and Wainwright, 1962), with the onset of hexagonal order.

Beyond the classification of the microstructure, one would like to understand how (dis)order affects the transport properties, like permeability, of the fibrous material. This is the topic of the next section.

4. Macroscopic properties

Recently, Yazdchi et al. (2012) showed that the mean values of the shortest Delaunay triangulation (DT) edges are nicely correlated with the macroscopic permeability at dilute and moderate porosities. In this section, we elaborate more on characterizing these channels (edges).

4.1. Effective channels based on Delaunay triangulations

Similar to Yazdchi et al. (2012), we define γ as the mean channel width (gap), i.e. surface-to-surface distance based on the shortest Delaunay edges $\langle e_t \rangle$, (averaged over Delaunay triangles) normalized by the fiber diameter, $\gamma = (\langle e_t \rangle - d)/d$. Fig. 7 shows these

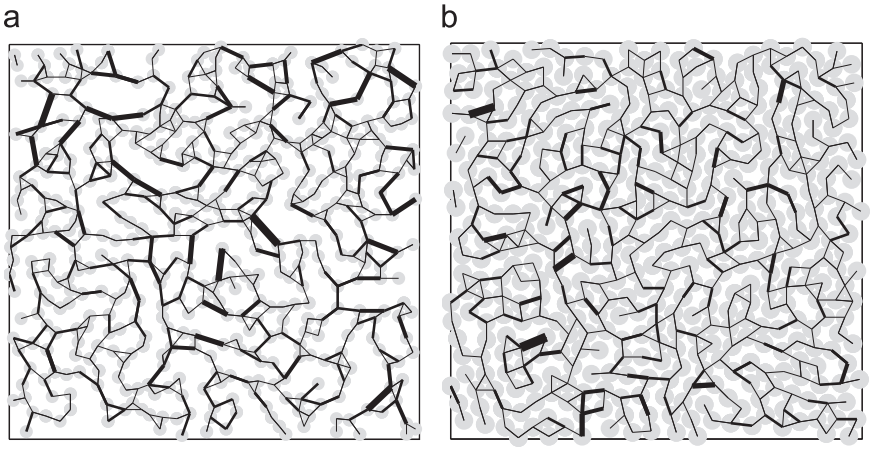

Fig. 7. The minimum Delaunay edges plotted for each Delaunay triangle for (a) dilute, $\varepsilon = 0.8$ and (b) dense, $\varepsilon = 0.4$ systems. The link between two particles is thicker when the channel is wider. Only the center part of the system is shown.

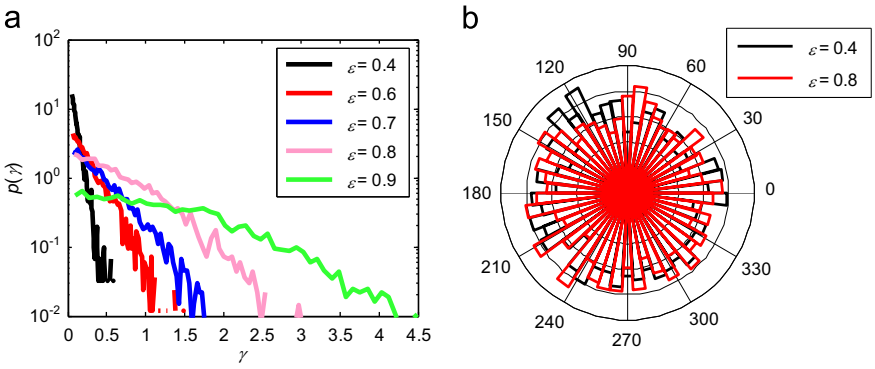

Fig. 8. (a) The probability distribution function of shortest Delaunay edges, γ at different porosities. (b) Polar histogram of the orientation of shortest Delaunay edges. All data are averaged over 10 realizations with 10^4 MC perturbations. (For interpretation of the references to color in this figure legend, the reader is referred to the web version of this article.).

shortest edges with channel width indicated by line thickness. These edges form a percolated edge-network channels through which the flow must go and, therefore correlate nicely with the permeability (see next section). Fig. 8 shows the PDF of widths and the histogram of the orientations of these channels. The distribution of the width of the channels, $p(\gamma)$ undergoes a transition from a very wide distribution to a narrower with increasing peak at lower γ, and eventually to a steep exponential distribution as the porosity decreases. For a perfect triangular lattice it reduces to exactly the inter-fiber (surface-to-surface) distance, i.e. $\gamma = \Delta_{\min} = 0.05$. The orientation of the channels is not much affected by the porosity and remains isotropic (no preferential direction) even for partially ordered structures at $\varepsilon = 0.4$.

4.2. Permeability calculation

Based on the Navier–Stokes equation, Gebart (1992) derived the permeability of an idealized unidirectional reinforcement consisting of regularly ordered, parallel fibers both for flow along and for flow perpendicular to the fibers. The solution for flow along fibers has the same form as the Carman–Kozeny (CK) equation (Yazdchi et al., 2011; Carman, 1937), while the solution for transverse flow has a different form

$$\frac{K}{d^2} = C\left(\sqrt{\frac{1-\varepsilon_o}{1-\varepsilon}}-1\right)^{2.5}, \tag{9}$$

where ε_o is the critical porosity below which there is no permeating flow and C is a geometric factor ($C\cong 0.1$, $\varepsilon_o \cong 0.2146$ for square and $C\cong 0.0578$, $\varepsilon_o \cong 0.0931$ for hexagonal arrays (Gebart, 1992)). Eq. (9) can be rewritten in terms of γ as

$$\frac{K}{d^2} = C\gamma^{2.5}, \tag{10}$$

which is exact for regular/ordered arrays and was shown to be valid also for disordered arrays at high and moderate porosities (Yazdchi et al., 2012), with $C\cong 0.2$. Relation (10) is remarkable, since it enables one to accurately determine the macroscopic permeability of a given packing just by averaging the narrowest Delaunay gaps, γ from Delaunay triangles. Fig. 9(a) shows the variation of the normalized permeability (in red) as a function of γ together with the local bond orientational order parameter, ψ_6^l (in blue points). The structural transition from disorder to order, indicated by strong increase in ψ_6^l, directly affects the macroscopic permeability. In disordered regimes, the permeability data nicely collapse on the theoretical power law relation (Eq. (10)). However, by appearance the local crystalline regions at $\varepsilon < 0.45$, the data start to deviate from the power law. In fact the lubrication theory, i.e. Eqs. (9) or (10), are only valid for perfectly ordered (hexagonal/square) or disordered (random) configurations with different pre-factor, C, in Eq. (10). Systems that are partially ordered have lower permeability compared to the predicted value in Eq. (10), i.e. $(K/d^2)_{ran}$, due to stagnancy of the fluid between fiber aggregates or within crystalline regions of close-by fibers. With decreasing porosity the data deviate from the solid line showing the appearance of ordering in the structure. In Yazdchi et al. (2012), we showed that this deviation can be represented by an exponential term

$$\frac{K}{d^2} = C\gamma^{2.5} g(\gamma) \text{ with } g(\gamma) = (1-g_0 e^{-m\gamma}), \quad g_0 \cong 0.5,\ m \cong 3 \tag{11}$$

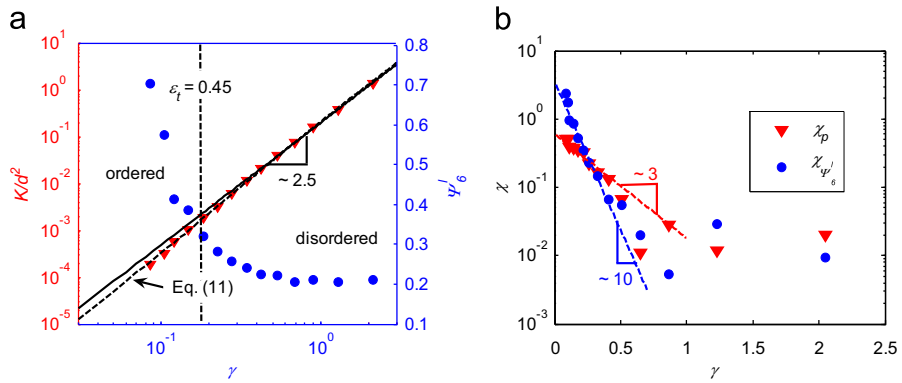

Fig. 9. (a) Variation of normalized permeability (red triangles, left axis) and local bond orientational parameter (blue dots, right axis) as function of mean shortest Delaunay gap length, γ. The solid line represents the power law, Eq. (10), obtained from the lubrication theory and the dashed line represents the corrected power law, Eq. (11), see Yazdchi et al. (2012). At the transition porosity $\varepsilon_t \cong 0.45$, the permeability data deviate considerably from the solid line power law for random structures. (b) Deviation of normalized permeability and local bond orientation order parameter from their random (disordered) values, i.e., $\chi_p = |1-K/K_{ran}|$ and $\chi_{\psi_6^l} = |1-\psi_6^l/(\psi_6^l)_{ran}|$, respectively, plotted against γ (For interpretation of the references to color in this figure legend, the reader is referred to the web version of this article.).

Fig. 9(b) shows that indeed, for both permeability and local bond orientation order parameter, this deviation, i.e., $\chi_p = |1-K/K_{ran}| \equiv g_0 e^{-m\gamma_2}$ and $\chi_{\psi_6^l} = |1-\psi_6^l/(\psi_6^l)_{ran}|$ respectively, can be well represented by an exponential term. The macroscopic permeability departs from the random prediction less strongly than the microscopic local bond order parameter—while both are functions of the Delaunay mean gap distance, γ. The numerical results show that the other micro-measures do not display this exponential deviation and, therefore, the local bond orientational order parameter seems better representing the transition from disordered to ordered configurations.

4.3. Further discussion and perspective for applications

Composite materials with various microstructures are ideally suited to achieve multifunctional features for the applications in modern technology at various length scales. Progress in our ability to synthesize composites or porous materials at a wide range of length scales and smart designing via computer simulations is expected to lead to new multifunctional materials. To our knowledge, there is so far no effective (semi)analytical method that can predict, with acceptable accuracy, the effective properties (such as permeability) of fibrous materials, while taking into account the effects of microstructure. To achieve a reliable prediction, one needs to work on a full description of the structural details of fibrous materials. However, it is extremely difficult, if not impossible, to completely describe the internal structure of a fibrous medium due to its complex and stochastic nature. Our study is only one step toward a more complete multi-scale modeling of realistic 3D random fibrous structures.

The simple microstructural relationships proposed here as predictions of the macroscopic permeability are remarkable: (i) they enable us to accurately determine the macroscopic permeability of a given packing just by measuring the 2nd narrowest channels (or equally the narrowest Delaunay edges), from only particle/fiber positions; (ii) they provide a powerful predictive tool for various fibrous product designs and performance optimizations; and (iii) they can be utilized to obtain simple (manufacturable) composite microstructures with targeted effective properties (Torquato et al., 2002, 2009). Such analyses will lead to more insights into the genesis of optimized microstructures and can be pursued in future work. Furthermore, our results can be used for calibration and validation of more advanced models for particle–fluid interactions within a multi-scale coarse graining and two-way coupled approach for moving fibers and deforming fiber-bundles, as carried out in our ongoing work (Srivastava et al., in preparation).

5. Darcy's law—upscaling the transport equations

The empirical Darcy's law, Eq. (1), is the key constitutive equation required to model up-scaled (under)ground water flow at low velocities and to predict the permeability of porous media. Though the volume-averaged equations, like Darcy's law, are used extensively in the literature, the method relies on length- and time-scale constraints which remain poorly understood. As shown in the previous section, the macroscopic transport properties, such as permeability, are linked to more fundamental equations describing the microscale behavior of fluids in porous materials, see also Bird et al. (2001) and Grouve et al. (2008).

In this section, we verify the validity of the macroscopic phenomenological Darcy's law at various length scales in a wide range of porosities. We recognize that the application of the pore-scale analysis requires characterization of the pore-scale geometry (and/or size) of the porous material. The Voronoi/Delaunay tessellation and their statistics are employed to obtain this essential geometrical (and/or length-scale) information.

5.1. Uniform cells

In order to study the validity of Darcy's law at different length scales, we divide our system into smaller uniform square cells as shown in Fig. 10(a) for porosity $\varepsilon = 0.6$. The corresponding fully resolved horizontal velocity field is shown in Fig. 10(b). Since we have sufficient number of elements between neighboring fibers, i.e. at least ~10 elements, all the velocity fluctuations and flow patterns can be captured at this length-scale. By upscaling (smoothing out) the velocity field, the permeability of each square cell, K_c can be calculated from Darcy's law, as

$$K_c = \frac{\mu U_c}{\nabla p_c}, \text{ with } U_c = \frac{1}{A_c}\sum_{e_c} u_{e_c} A_{e_c}, \quad A_c = a_c^2 \tag{12}$$

where U_c, a_c, e_c and $\nabla p_c = [(p_r^t + p_r^b)/2 - (p_l^t + p_l^b)/2]/a_c$ (t, b, r and l represent the pressure values at top, bottom, right and left sides of the cell, respectively) are average velocity, cell length, the elements within the cell and the pressure gradient for each individual cell, respectively. The variation of average cell velocity, U_c at porosity $\varepsilon = 0.6$ for the different cell areas, A_c normalized by the particle area, $A_p = \pi d^2/4$ is shown in Fig. 10(c) and (d) for $A_c/A_p \cong 20$ and $A_c/A_p \cong 160$, respectively. At higher resolutions, i.e. smaller

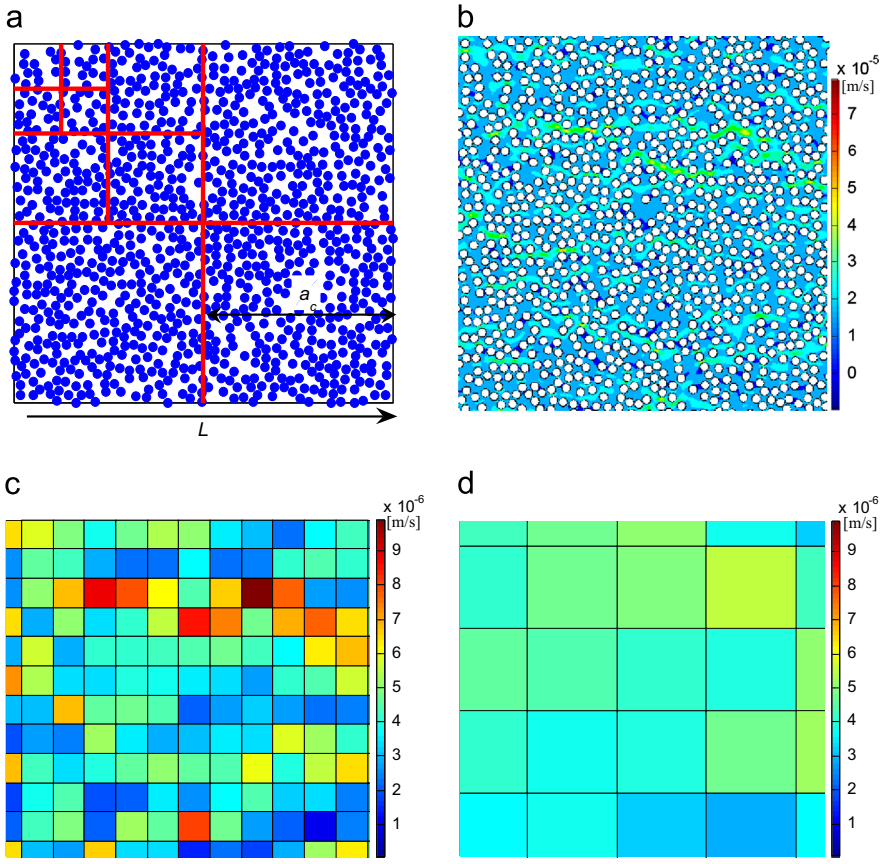

Fig. 10. (a) Center part of $N=3000$ randomly distributed fibers (particles) at porosity $\varepsilon=0.6$. The red cells show the various averaging cell areas; (b) the corresponding horizontal velocity field. The variation of average velocity, U_c at porosity $\varepsilon=0.6$ for the cell sizes of (c) $A_c/A_p\cong 20$, and (d) $A_c/A_p\cong 160$ (For interpretation of the references to color in this figure legend, the reader is referred to the web version of this article.).

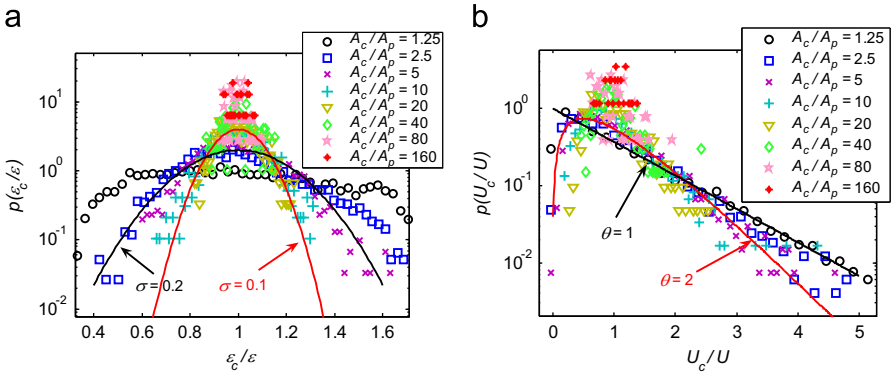

Fig. 11. (a) The PDF of the cell porosity, ε_c normalized with the macroscopic porosity, $\varepsilon=0.6$ at different resolutions. The solid lines show the best fitted Gaussian distribution, see Eq. (15) for $A_c/A_p=5$ (black line) and $A_c/A_p=20$ (red line). (b) The PDF of the cell average velocities, U_c normalized with the macroscopic or mean value, U at different resolutions at porosity $\varepsilon=0.6$. The solid lines show the best fitted gamma distribution, see Eq. (14) for $A_c/A_p=1.25$ (black line) and $A_c/A_p=5$ (red line) (For interpretation of the references to color in this figure legend, the reader is referred to the web version of this article.).

A_c/A_p, we see larger fluctuations (i.e. more flow heterogeneity/details) around the macroscopic average velocity, $U=4.07\times 10^{-6}$[m/s] obtained for the whole system, using the parameters specified in Section 2. This can be observed more clearly from the PDF of the cell average velocities, U_c at different resolutions as shown in Fig. 11(b). For small averaging cells, i.e. $A_c/A_p\sim 1$, the probability distribution of average cell velocities, $p(U_c)$ can be described by the two-parameter Gamma distribution as

$$p(U_c)=\frac{\lambda^\theta}{\Gamma(\theta)}U_c^{\theta-1}\exp(-\theta U_c),\quad \text{for } \theta,\lambda>0, \tag{13}$$

where θ and λ are, by definition, shape and scale parameters and $\Gamma(\theta)$ is the Gamma function.

The mean value of Gamma distributed average cell velocities is $\langle U_c\rangle=U=(\theta/\lambda)$. Written in terms of averaged velocity, $p(U_c)$ has only one free parameter which is

$$p\left(\frac{U_c}{U}\right)=\frac{\theta^\theta}{\Gamma(\theta)}\left(\frac{U_c}{U}\right)^{\theta-1}\exp\left(-\theta\left(\frac{U_c}{U}\right)\right),\quad \text{for } \theta>0. \tag{14}$$

The value of θ starts from $\theta=1$, i.e. exponential distribution, for small cell size, $A_c/A_p\cong 1$ (see the black line in Fig. 11(b)) and increases to ~3 for larger cell sizes, $A_c/A_p\cong 10$. For larger $A_c/A_p>20$, the $p(U_c/U)$ becomes more and more peaked and

narrower. The PDF of cell porosities, $p(\varepsilon_c/\varepsilon)$ at the macroscopic (average) porosity $\varepsilon=0.6$ is shown in Fig. 11(a). We observed that at small cell sizes, the $p(\varepsilon_c/\varepsilon)$ follows a uniform distribution, i.e. horizontal line. However, at larger resolutions, the $p(\varepsilon_c/\varepsilon)$ is fitted best by a Gaussian distribution as

$$p\left(\frac{\varepsilon_c}{\varepsilon}\right)=\frac{1}{\sigma\sqrt{2\pi}}\exp\left(-\frac{1}{2}\left(\frac{\varepsilon_c/\varepsilon-1}{\sigma}\right)^2\right), \tag{15}$$

where σ is the standard deviation of the data. By increasing the cell size, σ decreases till it becomes only scattered points around the mean value, i.e. $\varepsilon_c/\varepsilon\cong1$. Similar behavior and distributions were observed at different porosities (data not shown here). Note that at all cell lengths, the mean value of average cell velocity, $\langle U_c\rangle$ or pressure gradients, $\langle\nabla p_c\rangle$ are equal to their total average velocity, U or pressure gradient, ∇p (with maximum discrepancy of 2% due to ignoring the boundary elements and size effect, not shown here).

Knowing the average velocity and pressure gradient for each cell, one can calculate, from Eq. (12), the permeabilities for each individual cell as shown in Fig. 12(a) as scattered data for different porosities and cell sizes. The solid line shows the macroscopic permeability obtained for the whole system.

As expected, smaller cell areas lead to more scattered (fluctuating) permeabilities around the macroscopic value (black line). For sufficiently large cell sizes, i.e. $a_c\sim L$, the average of cell permeabilities, $\langle K_c\rangle$ approaches the macroscopic permeability, K obtained for the whole system. Fig. 12(b) shows the deviation of $\langle K_c\rangle$ from the macroscopic permeability plotted against normalized cell area, A_c/A_p at different porosities. By increasing the normalized area, the deviation decreases linearly with slope ~ −1. Interestingly, this trend is almost the same at all porosities.

In summary, the permeability for each cell is very sensitive to the averaging area with slow statistical convergence to the macroscopic value. Small areas, i.e. $A_c\sim A_p$, lead to more fluctuations in permeability in which the average, unlike velocity and porosity, will not approach the macroscopic value. Incorporating the observed distributions in a more accurate stochastic drag closure (or permeability) for advanced, coarse fluid-particle simulations is partly done in Srivastava et al. (in preparation) and can be further conducted in future.

5.2. Unstructured cells

To study the effect of shape of the averaging cell on the macroscopic permeability and averaging procedure, the Voronoi polygon and their dual graph, the Delaunay triangulations (DT), are employed as basic averaging area in this section.

The variation of average velocity at porosity $\varepsilon=0.6$ is shown in Fig. 13 using (a) Delaunay triangulation and (b) Voronoi polygons as averaging area. The average Voronoi area $\langle A_{VD}\rangle$ is always identical to the inverse of fiber density (number of fibers per unit area) equal to $\langle A_{VD}\rangle=0.5$. Similarly, the average Delaunay triangle area is half of the Voronoi areas, i.e. $\langle A_{DT}\rangle=\langle A_{VD}\rangle/2=0.25$. As expected using DT, due to smaller average cell area or higher resolution, one can capture more fluid details/heterogeneity and distinguish the dominant fluid channels.

The probability distribution function of cell porosities and average cell velocities at macroscopic porosity $\varepsilon=0.6$ is shown in Fig. 14. We observe that the PDF of the average cell porosity not only depends on the cell sizes but also on the shape of the cell area. Although the average cell area for both VD and DT are

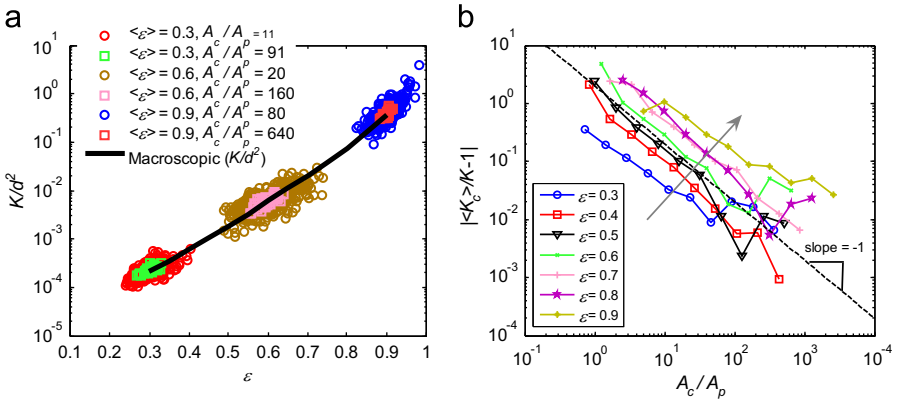

Fig. 12. (a) variation of normalized permeability as a function of porosity for various averaging cell sizes. The circles and squares correspond to $a_c/L\cong0.05$ and $a_c/L\cong0.15$, respectively. (b) Deviation of averaged permeability, $\langle K_c\rangle$ from macroscopic permeability, K as a function of normalized cell area at different porosities.

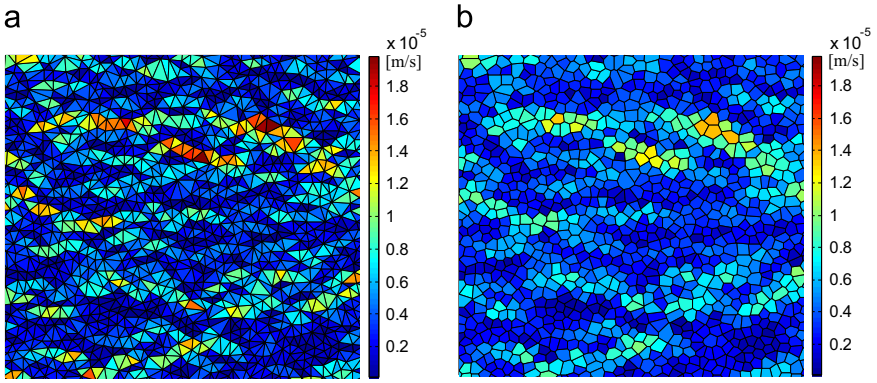

Fig. 13. Variation of average velocity at porosity $\varepsilon=0.6$ using (a) Delaunay triangulation and (b) Voronoi polygons as an averaging area.

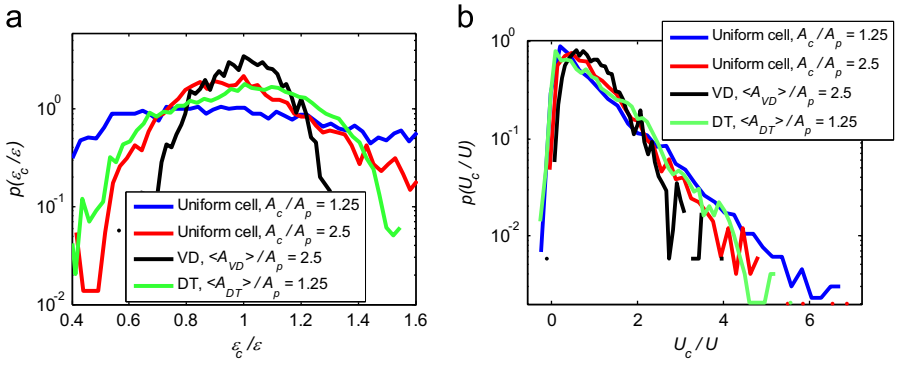

Fig. 14. The probability distribution function of (a) cell porosities and (b) average cell velocities at macroscopic porosity $\varepsilon = 0.6$. (For interpretation of the references to color in this figure legend, the reader is referred to the web version of this article.).

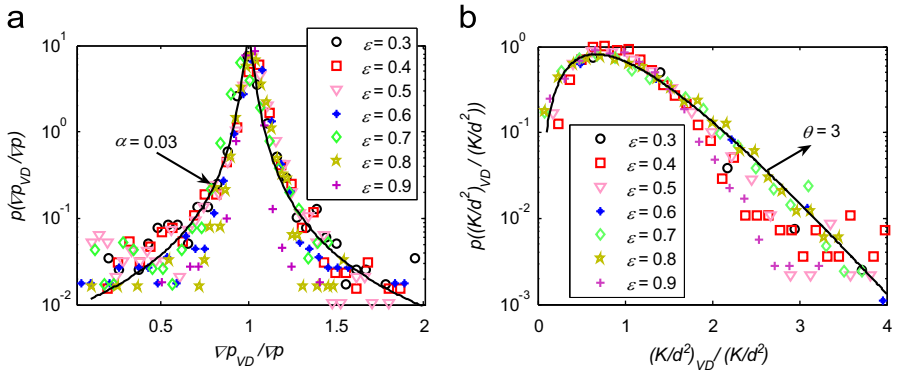

Fig. 15. The probability distribution function of Voronoi cell (a) pressure gradients and (b) normalized permeabilities at various porosities. The solid lines show the best Cauchy distribution, Eq. (16), and Gamma distribution, Eq. (14), at porosity $\varepsilon = 0.6$ in (a) and (b), respectively.

relatively small, however the PDF of cell porosities can be fitted by a Gaussian distribution, i.e. similar to larger uniform cell sizes. Surprisingly, the PDF of average cell velocities is not much affected by the cell shape/size and can be well approximated by a Gamma distribution for all VD, DT or uniform cells with $\theta \sim 1$, see Eq. (14).

Fig. 15 shows the PDF of (a) pressure gradients and (b) normalized permeabilities using Voronoi cells at various porosities. We observed that PDF of pressure gradients in Voronoi polygons follows a Cauchy distribution as

$$p\left(\frac{\nabla p_{VD}}{\nabla p}\right) = \frac{1}{\pi}\left(\frac{\alpha}{(\nabla p_{VD}/\nabla p - 1)^2 + \alpha^2}\right), \tag{16}$$

where α is the scale parameter and specifies the half-width at half-maximum (HWHM). For an infinitesimal scale parameter ($\alpha \sim 0$), the Cauchy distribution reduces to the Dirac delta function. However, the PDF of permeabilities within each Voronoi cell can be best fitted to a Gamma distribution. The both pressure gradient and permeability distributions seem to be weakly dependent on macroscopic porosity.

Similar to the analysis for uniform cells (Fig. 11), one can now define a coarse-grained length scale for Delaunay or Voronoi cells to investigate the evolution of distributions of pressure gradient or fluid velocity at coarser levels. This has been carrying out in our ongoing research.

6. Summary and conclusions

The transverse permeability for creeping flow through unidirectional (dis)ordered 1D an array of fibers/cylinders/discs has been studied numerically using the finite element method (FEM). Several micro-structural order parameters were introduced and employed to characterize the transition, controlled by the effective packing fraction, from disorder to partial order. In this context, the Voronoi and Delaunay diagrams are of interest as they provide information about nearest neighbors, gap distances and other structural properties of fibrous materials. In an ongoing research, the Delaunay triangulations have been also used both as a contact detection tool and a FE mesh in dense particulate flows (Srivastava et al., in preparation). Recently, we observed that the structural transition also affects the flow behavior at inertial (high Reynolds numbers) regimes (Yazdchi and Luding, 2012; Yazdchi, 2012; Narvaez et al., 2013).

The microstructure can be characterized by the means and distributions of local parameters, such as the number of faces, shape and regularity of Voronoi polygons, shortest Delaunay triangulation edges or gaps and local bond orientation measures. The numerical results show that the 3rd moment of the probability distribution of six-sided Voronoi polygons shows an increase at the transition porosity $\varepsilon_t^* \cong 0.39$. The average shape of the Voronoi polygons, $\langle\zeta\rangle$ increases almost linearly by increasing the porosity, regardless of the system size and packing generator algorithm. Furthermore, the average area moment of the Voronoi polygons, $\langle\Phi\rangle$ increases linearly by increasing the porosity with larger slope in the ordered case, relative to the disordered one.

The numerical experiments suggest a unique, scaling power law relationship between the permeability obtained from fluid flow simulations and the mean value of the shortest Delaunay triangulation gaps. Locally ordered regions, which cause a drop in the macroscopic permeability, can be detected by the local definition of the bond orientational order parameter, ψ_6^l. With decreasing porosity, both permeability and local bond orientational order parameter display an exponential deviation from the random case —where the bond order parameter deviation grows about three times faster.

Finally, the validity of the macroscopic Darcy's law at various length scales was studied using both uniform and Voronoi/Delaunay cells, in a wide range of porosities. We found universal but different distributions for pressure gradient and permeabilities using Voronoi polygons as an averaging area. The physical interpretation and correlation between these probabilities has to be addressed in the future, as the application of the proposed model/distributions for other macroscopic properties, like the heat conductivity. Moreover, the extension to real, non-parallel, deforming 3D structures of (possibly) moving fibers with friction and reptation remains a challenge for future work.

Acknowledgments

The authors would like to thank S. Srivastava, A.J.C. Ladd, P. Richard, K.W. Desmond and N. Rivier for helpful discussion and acknowledge the financial support of STW through the STW-MuST program, Project no. 10120.

References

Abate, A.R., Durian, D.J., 2006. Approach to jamming in an air-fluidized granular bed. Phys. Rev. E 74, 031308.
Alder, B.J., Wainwright, T.E., 1962. Phase transition in elastic disks. Phys. Rev. 127, 359–361.
Aurenhammer, F., 1991. Voronoi diagrams: a survey of a fundamental geometric data structure. ACM Comput. Surv. 23, 345–405.
Berg, M. de, Cheong, O., Kreveld, M. van, Overmars, M., 2008. Computational Geometry Algorithms and Applications. Springer-Verlag, Berlin.
Berryman, J.G., 1983. Random close packing of hard spheres and disks. Phys. Rev. A 27, 1053–1061.
Bird, R.B., Stewart, W.E., Lightfoot, E.N., 2001. Transport Phenomena, 2nd ed. John Wiley & Sons, US.
Bruschke, M.V., Advani, S.G., 1993. Flow of generalized Newtonian fluids across a periodic array of cylinders. J. Rheol. 37, 479–498.
Carman, P.C., 1937. Fluid flow through granular beds. Trans. Inst. Chem. Eng. 15, 150–166.
Chen, X., Papathanasiou, T.D., 2007. Micro-scale modeling of axial flow through unidirectional disordered fiber arrays. Compos. Sci. Technol. 67, 1286–1293.
Chen, X., Papathanasiou, T.D., 2008. The transverse permeability of disordered fiber arrays: a statistical correlation in terms of the mean nearest inter fiber spacing. Transport in Porous Media 71, 233–251.
Clague, D.S., Kandhai, B.D., Zhang, R., Sloot, P.M.A., 2000. Hydraulic permeability of (un)bounded fibrous media using the lattice Boltzmann method. Phys. Rev. E 61, 616–625.
Clusel, M., Corwin, E.I., Siemens, A.O.N., Brujic, J., 2009. A 'granocentric' model for random packing of jammed emulsions. Nature 460, 611–615.
Deen, N.G., Van Sint Annaland, M., Van der Hoef, M.A., Kuipers, J.A.M., 2007. Review of discrete particle modeling of fluidized beds. Chem. Eng. Sci. 62, 28–44.
Desch, C.H., 1919. The solidification of metals from the liquid state. J. Inst. Met. 22, 241.
Drummond, J.E., Tahir, M.I., 1984. Laminar viscous flow through regular arrays of parallel solid cylinders. Int. J. Multiphase Flow 10, 515–540.
Earnshaw, J.C., Harrison, M.B.J., Robinson, D.J., 1996. Local order in two-dimensional colloidal aggregation. Phys. Rev. E 53, 6155–6163.
Gebart, B.R., 1992. Permeability of unidirectional reinforcements for RTM. J. Compos. Mater. 26, 1100–1133.
Gervois, A., Annic, C., Lemaitre, J., Ammi, M., Oger, L., Troadec, J.-P., 1995. Arrangement of discs in 2d binary assemblies. Physica A 218, 403–418.
Gervois, A., Troadec, J.P., Lemaitre, J., 1992. Universal properties of Voronoi tessellations of hard discs. J. Phys. A Math. Gen. 25, 6169–6177.
Glazier, J.A., Gross, S.P., Stavans, J., 1987. Dynamics of two-dimensional soap froths. Phys. Rev. A 36, 306–312.
Grouve, W.J.B., Akkerman, R., Loendersloot, R., van den Berg, S., 2008. Transverse permeability of woven fabrics. Int. J. Mater. Form. (Suppl. 1), 859–862.
Halperin, B.I., Nelson, D.R., 1978. Theory of two-dimensional melting. Phys. Rev. Lett. 41, 121–124.
Happel, J., 1959. Viscous flow relative to arrays of cylinders. AIChE 5, 174–177.
Jackson, G.W., James, D.F., 1986. The permeability of fibrous porous media. Can. J. Chem. Eng. 64 (3), 364–374.
Jaganathan, S., Vahedi Tafreshi, H., Pourdeyhimi, B., 2008. A realistic approach for modeling permeability of fibrous media: 3-D imaging coupled with CFD simulation. Chem. Eng. Sci. 63, 244–252.
Jaster, A., 1999. Computer simulations of the two-dimensional melting transition using hard disks. Phys. Rev. E 59, 2594–2602.
Kansal, A.R., Truskett, T.M., Torquato, S., 2000. Nonequilibrium hard-disk packings with controlled orientational order. J. Chem. Phys. 113, 4844–4851.
Katz, A.J., Thompson, A.H., 1986. Quantitative prediction of permeability in porous rocks. Phys. Rev. B 34, 8179–8181.
Kawasaki, T., Onuki, A., 2011. Construction of a disorder variable from Steinhardt order parameters in binary mixtures at high densities in three dimensions. J. Chem. Phys. 135, 174109.
Kumar, V.S., Kumaran, V., 2005. Voronoi neighbor statistics of hard-disks and hard-spheres. J. Chem. Phys. 123, 074502.
Kumar, V.S., Kumaran, V., 2006. Bond-orientational analysis of hard-disk and hard-sphere structures. J. Chem. Phys. 124, 204508.
Kuwabara, S., 1959. The forces experienced by randomly distributed parallel circular cylinders or spheres in a viscous flow at small Reynolds numbers. J. Phys. Soc. Jpn. 14, 527–532.
Lage, J.L., Antohe, B.V., 2000. Darcy's experiments and the deviation to nonlinear flow regime. J. Fluids Eng. 122, 619–625.
Le Caer, G., Delannay, R., 1993. Correlations in topological models of 2D random cellular structures. J. Phys. A Math. Gen. 26, 3931–3954.
Lemaítre, J., Troadec, J.P., Gervois, A., Bideau, D., 1991. Experimental study of densification of disc assemblies. Europhys. Lett. 14, 77–83.
Lemaítre, J., Gervois, A., Troadec, J.P., Rivier, N., Ammi, M., Oger, L., Bideau, D., 1993. Arrangement of cells in Voronoi tesselations of monosize packing of discs. Philos. Mag. Part B 67, 347–362.
Lewis, F.T., 1931. A comparison between the mosaic of polygons in a film of artificial emulsion and the pattern of simple epithelium in surface view (cucumber epidermis and human amnion). Anat. Rec. 50, 235–265.
Mattern, K.J., Deen, W.M., 2007. Mixing rules for estimating the hydraulic permeability of fiber mixtures. AIChE J. 54 (1), 32–41.
Mei, C.C., Auriault, J.-L., 1991. The effect of weak inertia on flow through a porous medium. J. Fluid Mech. 222, 647–663.
Miklius, M.P., Hilgenfeldt, S., 2012. Analytical results for size-topology correlations in 2D disk and cellular packings. Phys. Rev. Lett. 108, 015502.
Moucka, F., Nezbeda, I., 2005. Detection and characterization of structural changes in the hard-disk fluid under freezing and melting conditions. Phys. Rev. Lett. 94, 040601.
Narvaez, A., Yazdchi, K., Luding, S., Harting, J., 2013. From creeping to inertial flow in porous media: a lattice Boltzmann-finite element study. J. Stat. Mech., P02038.
Oger, L., Gervois, A., Troadec, J.P., Rivier, N., 1996. Voronoi tessellation of packings of spheres: topological correlation and statistics. Philos. Mag. B 74, 177–197.
Okabe, A., Boots, B., Sugihara, K., 1992. Spatial Tessellations: Concepts and Applications of Voronoi Diagrams. John Wiley & Sons, UK.
Papathanasiou, T.D., 1996. A structure-oriented micromechanical model for viscous flow through square arrays of fiber clusters. Compos. Sci. Technol. 56, 1055–1069.
Pittet, N., 1999. Dynamical percolation through the Voronoi tessellations. J. Phys. A Math. Gen. 32, 4611–4621.
Quilliet, C., Ataei Talebi, S., Rabaud, D., Kafer, J., Cox, S.J., Graner, F., 2008. Topological and geometrical disorders correlate robustly in two-dimensional foams. Philos. Mag. Lett. 88, 651–660.
Reis, P.M., Ingale, R.A., Shattuck, M.D., 2006. Crystallization of a quasi-two-dimensional granular fluid. Phys. Rev. Lett. 96, 258001.
Richard, P., Oger, L., Troadec, J.-P., Gervois, A., 1999. Geometrical characterization of hard-sphere systems. Phys. Rev. E 60, 4551–4558.
Richard, P., Oger, L., Troadec, J.P., Gervois, A., 1998. Tessellation of binary assemblies of spheres. Physica A 259, 205–221.
Rintoul, M.D., Torquato, S., 1996. Computer simulations of dense hard-sphere systems. J. Chem. Phys. 105, 9258–9265.
Rivier, N., 1994. Maximum entropy for random cellular structures. In: Grassberger, Peter, Nadal, Jean-Pierre, (Eds.), From Statistical Physics to Statistical Inference and Back, NATO Science Series, vol. 428. Publisher: Springer, Netherlands, pp. 77–93.
Sangani, A.S., Acrivos, A., 1982. Slow flow past periodic arrays of cylinders with application to heat transfer. Int. J. Multiphase Flow 8, 193–206.
Sangani, A.S., Yao, C., 1988. Transport processes in random arrays of cylinders. 2: viscous-flow. Phys. Fluids 31 (9), 2435–2444.
Schliecker, G., 2002. Structure and dynamics of cellular systems. Adv. Phys. 51, 1319–1378.
Smith, C.S., 1954. The shape of things. Sci. Am. 190, 58–64.
Sobera, M.P., Kleijn, C.R., 2006. Hydraulic permeability of ordered and disordered single-layer arrays of cylinders. Phys. Rev. E 74 (3), 036302.
Srivastava, S., Yazdchi, K., Luding, S., in preparation. Meso-scale coupling of FEM/DEM for fluid-particle interactions.
Stylianopoulos, T., Yeckel, A., Derby, J.J., Luo, X-J., Shephard, M.S., Sander, E.A., Barocas, V.H., 2008. Permeability calculations in three-dimensional isotropic and oriented fiber networks. Phys. Fluids 20, 123601.
Tamayol, A., Bahrami, M., 2011. Transverse permeability of fibrous porous media. Phys. Rev. E 83 (4), 046314.
Tomadakis, M.M., Robertson, T.J., 2005. Viscous permeability of random fiber structures: comparison of electrical and diffusional estimates with experimental and analytical results. J. Compos. Mater. 39 (2), 163–188.
Tomadakis, M.M., Sotirchos, S.V., 1993. Transport properties of random arrays of freely overlapping cylinders with various orientation distributions. J. Chem. Phys. 98 (1), 616–626.
Torquato, S., Hyun, S., Donev, A., 2002. Multifunctional composites: optimizing microstructures for simultaneous transport of heat and electricity. Phys. Rev. Lett. 89, 266601.
Torquato, S., 2009. Inverse optimization techniques for targeted self-assembly. Soft Matter 5, 1157–1173.

Tsumuraya, K., Ishibashi, K., Kusunoki, K., 1993. Statistics of Voronoi polyhedra in a model silicon glass. Phys. Rev. B 47, 8552–8557.
Valdes-Parada, F.J., Ochoa-Tapia, J.A., Alvarez-Ramirez, J., 2009. Validity of the permeability Carman Kozeny equation: a volume averaging approach. Physica A 388, 789–798.
Wang, Z., Alsayed, A.M., Yodh, A.G., Han, Y., 2010. Two-dimensional freezing criteria for crystallizing colloidal monolayers. J. Chem. Phys. 132, 154501.
Whitaker, S., 1986. Flow in porous media I: a theoretical derivation of Darcy's law. Transp. Porous Media 1, 3–25.
Yazdchi, K., Srivastava, S., Luding, S., 2011. Microstructural effects on the permeability of periodic fibrous porous media. Int. J. Multiphase Flow 37, 956–966.
Yazdchi, K., Srivastava, S., Luding, S., 2012. Micro–macro relations for flow through random arrays of cylinders. Composites Part A 43, 2007–2020.
Yazdchi, K., Luding, S., 2012. Towards unified drag laws for inertial flow through fibrous materials. Chem. Eng. J. 207, 35–48.
Yazdchi, K., 2012. Micro–macro relations for flow through fibrous media, Ph.D. thesis, University of Twente, The Netherlands.
Yu, D.-Q., Chen, M., Han, X.-J., 2005. Structure analysis methods for crystalline solids and supercooled liquids. Phys. Rev. E 72, 051202–051207.
Zheng, X.H., Earnshaw, J.C., 1995. Plasma-dust crystals and Brownian motion. Phys. Rev. Lett. 75, 4214–4217.
Zhu, H.P., Zhou, Z.Y., Yang, R.Y., Yu, A.B., 2008. Discrete particle simulation of particulate systems: a review of major applications and findings. Chem. Eng. Sci. 63, 5728–5770.
Zhu, H.X., Thorpe, S.M., Windle, A.H., 2001. The geometrical properties of irregular two-dimensional Voronoi tessellations. Philos. Mag. A 81, 2765–2783.